Three-dimensional analysis of eccentric pounding between two-storey structures using explicit non-smooth dynamics

José Henrique Krahenbuhl Ambiel, Michael Brun, Alfred Thibon, Anthony Gravouil

Three-dimensional analysis of eccentric pounding between two-storey structures using explicit non-smooth dynamics

José Henrique Krahenbuhl Ambiel [b,c], Michael Brun [a,*], Alfred Thibon [d], Anthony Gravouil [c]

[a] Université de Lorraine, Arts et Métiers Paris Tech, CNRS, LEM3, Metz F-57000, France
[b] GEOMAS, INSA de Lyon, 17 rue des Arts, F-69621 Villeurbanne, France
[c] LaMCoS, INSA de Lyon, Université de Lyon, CNRS UMR5259, 18-20 rue des Sciences, F-69621 Villeurbanne, France
[d] Direction Technique, SAE/DS, EDF/DIPNN, 19 rue Pierre Bourdeix, 69007 Lyon, France

ARTICLE INFO

Keywords:
Structural pounding
Explicit non-smooth dynamics
Lagrange multipliers
3D FEM analysis
Floor response spectra

ABSTRACT

Pounding research has been gaining momentum in the last decades with large earthquakes hitting cities with insufficiently separated buildings. Even if no major structural damage may be observed in the case of slab–slab pounding, large acceleration pulses may influence the response of equipment and cause disruption in their functionality. In this work, two different models are set up for reproducing shake table tests concerning two-storey adjacent structures, with slab–slab pounding. For the slab representation, the first model uses hexahedral finite elements, while the second one uses shell elements. One of the main objectives of the study is to predict the floor response spectra over a broad frequency range, up to 400Hz. Transient computations of the pounding problem under earthquake excitation are carried out using the explicit CD-Lagrange approach. Rayleigh damping is employed to filter out the spurious high frequency oscillations. The comparison between numerical and experimental results in terms of displacements and floor acceleration spectra shows that the numerical models are able to reproduce the eccentric pounding during the shake table tests. No parameter adjustment related to the contact is required underlining the robustness of the approach.

1. Introduction

Pounding has been gaining attention of structural engineers and researchers over the last decades due to large earthquakes hitting the cities. The collision between structures, in the worst case, can lead them to total collapse as observed during the earthquake in Mexico City in 1985 [1]. When there is no collapse, the effects of pounding can vary from architectural damage to major structural problems [2–4]. Furthermore, even when pounding does not result in severe structural damage, it can be harmful to building equipment as observed in a pounding survey concerning the 1989 Loma Prieta earthquake [5]. Indeed, mechanical solicitations from impacts between adjacent buildings are characterized by short duration acceleration pulses with a high frequency content. These high frequencies can disrupt the functionality of some buildings content, for example, nuclear power plant equipment such as electrical cabinets. The influence of pounding on the floor response spectra is the main concern of this work, requiring to adopt a detailed 3D analysis in order to represent eccentric pounding occurring between the slabs of the adjacent buildings.

Several numerical methods have been proposed in the literature in order to better understand the complexity of pounding. The single-degree-of-freedom (SDOF) model of colliding structures has been adopted in various works. Taking advantage of this simplified representation, parametric and sensitivity analyses have been carried out to derive the most influential parameters [6–8]. The numerical approach for modeling the impact usually employed contact element based on Hertz contact. Anagnostopoulos used SDOF systems to study series of several buildings in a city block, analyzing a wide range of parameters [9]. The same city block was studied by Athanassiadou et al. but considering a time lag in the earthquake excitation for the different oscillators so as to roughly model the traveling wave effect [10]. Davis [11] analyzed a SDOF oscillator impacting a rigid neighboring structure. Naderpour and co-authors studied the influence of various parameters related to the contact element and concluded that gap between structures, coefficient of restitution, impact velocity and stiffness of contact element have a strong influence on the output parameters [12,13]. Nonetheless, SDOF models cannot represent the different vibration modes of the colliding structures. More detailed

analysis have been carried out on multi-degree-of-freedom (MDOF) systems to determine the most unfavorable conditions in relation to pounding and its damaging consequences [14]. The effect of the initial gap influence, the building relative frequencies and the characteristics of the contact element have been investigated in parametric studies [15–18]. Slab-slab pounding produces high magnitude and short duration floor acceleration pulses as well as increased shear force at various storey levels in comparison to the no-pounding case. The worst case where the floor of a building collides against the column of the adjacent one has been considered by Karayannis et al. [19] and Favvata et al. [20,21] in order to assess the high ductility demand of critical columns. A MDOF model was also adopted by Wolf et al. to investigate the pounding between a nuclear reactor and an adjacent structure [22]. The authors observed that high frequency modes are strongly excited and concluded that pounding can increase the high frequency range of the response spectra inside the structure. The study of pounding between a 15-floor building and an 8-floor one was conducted by Kasai et al. with MDOF systems [5]. The authors observed that the peak floor acceleration at the pounding level can be more than 10 times compared to the case without pounding. Moreover, the floor acceleration response spectra are also amplified by a factor of 10 in the high frequency range, reaching even 30 at some frequencies, thus potentially harmful to equipment or secondary systems having short periods.

The eccentric seismic pounding plays a fundamental role for an accurate simulation of the amplification of floor response spectra. Leibovich et al. investigated the eccentric pounding with a simple model including a rotational degree of freedom [23]. A more refined model was proposed by Papadrakakis et al. with 3D structures modeled with beam elements and rigid floors concerned by the slab-slab impacts with neighboring structures [24]. The flexibility of the slabs as well as non-linear material behavior have been taken into account in a more complex Finite Element (FE) analysis by Jankowski [25], using shell elements, to simulate the pounding between the Olive View Hospital main building and one of its independently standing stairway towers. More recently, Karayannis and Naoum also studied the torsional behavior of RC frame structure due to assymetric pounding using 3D beam-elements and lumped plasticity [26]. By considering a detailed three-dimensional model with shell elements and non-linear material behavior, Bi and Hao simulated the pounding damage to bridge structures by taking into account eccentric impacts between girders [27]. Crozet et al. adopted a three-dimensional model to reproduce the shake table tests conducted on two representative scale adjacent structures subject to pounding, and then, on the basis of the set up 3D model, adopted a simplified model by taking into account the first six eigenmodes for each structure [28,29]. The experimental campaign carried out on the main shake table of the French Commissariat à l'Energie Atomique (CEA) in Saclay, France, mainly focused on the pounding influence on the floor response spectra [30]. The very substantial numerical results provided by this experimental campaign allow us to validate the numerical approach proposed in this work

Explicit time integration for pounding using Lagrange multipliers is prone to generate spurious high frequency oscillations due to the high frequency modes contained in a refined FE mesh. Such high frequency oscillations require to be damped out to avoid the complete blur of the structure response.

In this paper, the time integration of the equation of motion is done with the explicit Central Difference (CD) scheme and the contact/impact conditions are handled by the CD-Lagrange algorithm which imposes the contact/impact conditions in a velocity-impulse format via Lagrange multipliers [35]. This approach was also validated in a series of benchmarks in non-smooth transient dynamics [36] and used for Rate and State frictional contact [37]. As the main purpose of this work is to accurately predict the floor response spectra, special attention should be paid to the numerical approach to introduce a sufficient damping without altering the spectral accelerations over a broad frequency range. Classical Rayleigh damping, including both mass and stiffness contributions, is adopted in the pounding simulations to filter out the high frequency oscillations generated by the impacts.

In the following, three-dimensional FE analyses are carried out to reproduce the results of the experimental campaign conducted by Crozet et al. [28,30] in terms of displacements, accelerations and floor response spectra. In this experimental campaign, the case of pounding between two structures, impacting at their first and second floors, is investigated. Three different gap values between the structures were tested for four excitation signals. The eccentric pounding between the slabs is reproduced using two different models: the first one adopts shell element for the slabs, with edge-to-edge impact, whereas the second model adopts solid elements with face-to-face impact, to better reproduce the time history of the complex pounding phenomena between the two slabs.

Section 2 presents the equations on which this work is based, in particular the explicit CD-Lagrange scheme with Rayleigh damping. In Section 3, the construction of the two numerical models for the adjacent structures is presented as well as the damping parameters. The results are exhibited in Section 4, demonstrating the ability of the set up models to accurately reproduce the complex eccentric pounding phenomena in terms of displacements, accelerations and especially in terms of floor response spectra which is the special focus of this work. Finally, the conclusions and main perspectives of this work are drawn in Section 5.

2. Methods

In this section, we summarize the formulation developed in [35] for explicit contact dynamics, called CD-Lagrange time integrator. The strong and the weak form of the problem with the Hertz–Signorini–Moreau (HSM) contact conditions are first introduced. After classical FE discretization, the Lagrange multipliers allow us to ensure the impact/contact conditions according to the velocity-impulse format as proposed by Moreau [38,39]. We employ Rayleigh damping with stiffness matrix contribution to filter out the high frequency oscillations due to the impacts and the space discretization of the colliding structures. As underlined by Belytschko, the Rayleigh viscous matrix with stiffness contribution leads to the decrease of the time step when using explicit Central Difference method [40]. This aspect will be handled in the following section by computing the maximal angular frequency of the FE model so as to ensure the stability of the CD-Lagrange scheme.

2.1. HSM contact conditions

Two deformable bodies Ω_1 and Ω_2 are considered, as depicted in Fig. 1, with initial and deformed configurations. Ω_1 and Ω_2 belong to $\mathbb{R}^d$ with regular boundaries, d being the number of space dimensions assumed to be equal to 3 in the following. On the body boundaries, denoted by Γ_1 and Γ_2, three distinct fields are distinguished: Γ_{D_1} and Γ_{D_2} for Dirichlet conditions, Γ_{N_1} and Γ_{N_2} for Neumann conditions and

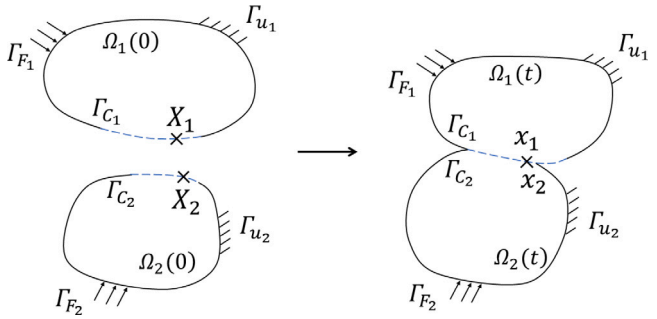

Fig. 1. Two deformable bodies in contact, Ω_1 being the master body and Ω_2 the slave body.

Γ_{C_1} and Γ_{C_2} for the contact interface between the two bodies. For a pair of contact points, $\underline{X}_k$ belonging to the contact interface Γ_{C_k} $(k = 1, 2)$, the HSM conditions for a frictionless contact, under the small displacement assumption, are written as:

$$\begin{cases} g_N = [(\underline{X}_2 + \underline{u}_2) - (\underline{X}_1 + \underline{u}_1)] \cdot \underline{n}_1 \geq 0 \\ \tau_N = \underline{\underline{\sigma}}_k \cdot \underline{n}_k \cdot \underline{n}_k \leq 0 \quad , \quad k = 1, 2 \\ g_N \cdot \tau_N = 0 \end{cases} \tag{1}$$

with g_N the gap between the two points of the contact interface and the displacements $\underline{u}_1$ and $\underline{u}_2$ of the two contact points. The normal stress is represented by τ_N, $\underline{\underline{\sigma}}_k$ is the stress tensor at the contact points and $\underline{n}_k$ the normal to the surface at the contact points. The first inequality is the condition of impenetrability, *i.e.* bodies cannot occupy the same point at the same time. The second inequality imposes that the normal contact stress τ_N is always negative, *i.e.* that only compression is possible between the bodies. Finally, the third condition imposes that there is compression only when the bodies are in contact and also that the work done by the contact forces is zero. According to Moreau's lemma of viability [39], it is also possible to write the contact conditions in Eq. (1) in terms of velocity given by:

$$\begin{cases} \text{if} \quad g_N > 0 \quad \text{then} \quad i_N = 0 \\ \text{if} \quad g_N = 0 \quad \text{then} \quad \begin{cases} \dot{g}_N \geq 0 \\ i_N \leq 0 \\ \dot{g}_N \cdot i_N = 0 \end{cases} \end{cases} \tag{2}$$

where i_N is the contact impulse; $\dot{g}_N$ is the normal component of the relative velocity between the two points, *i.e.* the gap velocity, defined as:

$$\dot{g}_N = (\dot{\underline{u}}_2 - \dot{\underline{u}}_1) \cdot \underline{n}_1 \tag{3}$$

with $\dot{\underline{u}}_1$ and $\dot{\underline{u}}_2$ the velocity of the two contact points.

2.2. Strong formulation

We note Ω such that $\Omega = \Omega_1 \cup \Omega_2$ and Γ_C refers to all the contact interfaces: $\Gamma_C = \Gamma_{C_1} \cup \Gamma_{C_2}$. Similarly, all the interfaces with Dirichlet conditions are denoted by $\Gamma_D = \Gamma_{D_1} \cup \Gamma_{D_2}$ and all the interfaces with Neumann conditions are denoted by $\Gamma_N = \Gamma_{N_1} \cup \Gamma_{N_2}$. In addition to the small displacement assumption, the materials are assumed to be linear elastic. The mechanical behavior of both deformable bodies is governed by the equilibrium equation completed with the HSM conditions as shown below:

$$\begin{cases} \underline{div}(\underline{\underline{\sigma}}) + \underline{b} = \rho \ddot{\underline{u}} & \text{in } \Omega \\ \underline{\underline{\sigma}} = \underline{\underline{\underline{\underline{C}}}} : \underline{\underline{\epsilon}} & \text{in } \Omega \\ \underline{\underline{\epsilon}} = \frac{1}{2}[\underline{\underline{grad}}(\underline{u}) + \underline{\underline{grad}}(\underline{u})^T] & \text{in } \Omega \\ \underline{u} = \underline{u}_D & \text{on } \Gamma_D \\ \underline{\underline{\sigma}} \cdot \underline{n} = \underline{t}_N & \text{on } \Gamma_N \\ \text{HSM contact conditions} & \text{on } \Gamma_C \end{cases} \tag{4}$$

$\underline{b}$ being the volumetric force, $\underline{\underline{\sigma}}$ the stress tensor, $\underline{\underline{\epsilon}}$ the deformation tensor, $\underline{\underline{\underline{\underline{C}}}}$ the constitutive tensor, $\underline{u}_D$ the prescribed displacements and $\underline{t}_N$ the prescribed surface forces.

2.3. Weak formulation

The solutions $\underline{u}_1(t)$ and $\underline{u}_2(t)$ in subdomains Ω_1 and Ω_2 are sought in the appropriate spaces $V_1 = \{\underline{u}_1 \in [H^1(\Omega_1)]^d : \underline{u}_1 = \underline{u}_1^D \ \ on \ \ \Gamma_1^D\}$ and $V_2 = \{\underline{u}_2 \in [H^1(\Omega_2)]^d : \underline{u}_2 = \underline{u}_2^D \ \ on \ \ \Gamma_2^D\}$, respectively, whereas the test space functions $\underline{v}_1$ and $\underline{v}_2$ belong to the spaces V_1^0 and V_2^0, satisfying the zero value at the Dirichlet conditions. At the contact interface, we consider the Lagrange multipliers $\underline{\lambda}$ as well as its related test functions $\underline{\mu}$, belonging to the appropriate spaces, corresponding to the adapted dual trace space denoted by M.

The virtual work for transient dynamics problems can be written for the two subdomains: $\forall t \in [0, T]$, find $\underline{u}_1(t) \in V_1$, $\underline{u}_2(t) \in V_2$, $\underline{\lambda}(t) \in M$, such that the following weak form is satisfied $\forall \underline{v}_1 \in V_1^0$, $\forall \underline{v}_2 \in V_2^0$, $\forall \underline{\mu} \in M$:

$$\begin{aligned} &\int_{\Omega_1} \rho_1 \underline{v}_1 \cdot \ddot{\underline{u}}_1 d\Omega + \int_{\Omega_1} \underline{\underline{\epsilon}}(\underline{v}_1) : \underline{\underline{\sigma}}_1 \, d\Omega \\ &\qquad + \int_{\Omega_2} \rho_2 \underline{v}_2 \cdot \ddot{\underline{u}}_2 d\Omega + \int_{\Omega_2} \underline{\underline{\epsilon}}(\underline{v}_2) : \underline{\underline{\sigma}}_2 \, d\Omega \\ &= \int_{\Omega_1} \underline{v}_1 \cdot \underline{b}_1 d\Omega + \int_{\Omega_2} \underline{v}_2 \cdot \underline{b}_2 d\Omega + \int_{\Gamma_{N_1}} \underline{v}_1 \cdot \underline{g}_{N_1} d\Gamma \\ &\qquad + \int_{\Gamma_{N_2}} \underline{v}_2 \cdot \underline{g}_{N_2} d\Gamma + \\ &\qquad \int_{\Gamma_C} (\underline{v}_2 - \underline{v}_1) \cdot \underline{\lambda} \, d\Gamma + \int_{\Gamma_C} \underline{\mu} \cdot (\dot{\underline{u}}_1 - \dot{\underline{u}}_2) d\Gamma \end{aligned} \tag{5}$$

with $\underline{\lambda}$ the Lagrange multipliers, and $\underline{\mu}$ the weight functions related to Lagrange multipliers. The HSM contact conditions for normal velocities are prescribed in weak form by the term $\int_{\Gamma_C} \underline{\mu} \cdot (\dot{\underline{u}}_1 - \dot{\underline{u}}_2) d\Gamma$. The term $\int_{\Gamma_C} (\underline{v}_2 - \underline{v}_1) \cdot \underline{\lambda} \, d\Gamma$ corresponds to the contact energy.

2.4. CD-Lagrange scheme with Rayleigh damping

We use the Finite Element Method for the spatial discretization. A restriction operator, denoted by $\mathbf{L}_N$, is also introduced which selects the degrees of freedom involved in the contact such as: $\dot{\mathbf{g}}_N = \mathbf{L}_N \dot{\mathbf{U}}$, with $\dot{\mathbf{U}}$ the relative velocity vector for the two bodies.

From the weak formulation of the problem in Eq. (5), we write the discrete equations in space and time according to the explicit Central Difference scheme on the time step $\Delta t = [t_n; t_{n+1}]$ as:

$$\begin{cases} \mathbf{M}\ddot{\mathbf{U}}_{n+1} + \mathbf{C}\dot{\mathbf{U}}_{n+1/2} + \mathbf{K}\mathbf{U}_{n+1} = \mathbf{f}_{ext,n+1} + \mathbf{f}_{cont,n+1} \\ + \text{ HSM contact conditions} \end{cases} \tag{6}$$

with $\mathbf{M}$ the lumped mass matrix, $\mathbf{C}$ the damping matrix, $\mathbf{K}$ the stiffness matrix, $\mathbf{f}_{ext,n+1}$ the external forces, $\mathbf{f}_{cont,n+1}$ the contact forces and $\mathbf{U}_{n+1}$, $\dot{\mathbf{U}}_{n+1/2}$ and $\ddot{\mathbf{U}}_{n+1}$ the displacements, velocities and accelerations for the two bodies. It can be noted that the damping matrix operates on the mid-step velocities, at $t_{n+1/2}$, so as to provide a fully-explicit formulation for the Central Difference scheme [40]. Here the adopted damping matrix is the classical Rayleigh viscous damping matrix, defined as: $\mathbf{C} = \alpha\mathbf{M} + \beta\mathbf{K}$, where the parameters α and β have to be chosen as a function of the target damping ratios at two frequencies of each structure [25]. It is important to underline that stiffness matrix contribution in the damping matrix is mandatory to filter out the spurious high

frequencies. Indeed, without this stiffness contribution, the solution can be completely blurred by high-frequency vibration modes contained in the refined mesh, and excited by the use of Lagrange multipliers for reproducing the non-smooth dynamics. Rayleigh viscous matrix with a stiffness matrix term is efficient to damp out the high frequency oscillations generated by the Lagrange multipliers, without altering the accuracy of accelerations over a broad range of frequencies. However, it leads to a decrease of the critical time step when using the Central Difference scheme, due to the time lag introduced in the viscous terms in the discrete equation of motion in Eq. (6) [40]. In the following section, this decrease of the critical time step is accurately assessed by computing the maximal angular frequency of the structure model. Another way to control the spurious numerical oscillations inherent to the use of Lagrange multipliers is to use explicit time integration scheme with numerical damping such as the explicit α-generalized scheme [41] or explicit Noh–Bathe scheme [42], but with the difficulty of tuning the time integration parameters for the investigated complex pounding situation. To handle the contact, we use the approach proposed by [35], based on the velocity-impulse formulation, written at time $t_{n+3/2}$. This approach is inspired by the works of Moreau and Jean [38,39,43]. Thus we multiply the equation of motion in Eq. (6) by the time step Δt and we use the Central Difference approximation for the acceleration: $\ddot{\mathbf{U}}_{n+1} = \frac{\dot{\mathbf{U}}_{n+3/2} - \dot{\mathbf{U}}_{n+1/2}}{\Delta t}$. It leads to the following expression:

$$\mathbf{M}\dot{\mathbf{U}}_{n+3/2} = \mathbf{M}\dot{\mathbf{U}}_{n+1/2} + \Delta t \left(\mathbf{f}_{ext,n+1} - \mathbf{C}\dot{\mathbf{U}}_{n+1/2} - \mathbf{K}\mathbf{U}_{n+1}\right) + \mathbf{I}_{n+1} \tag{7}$$

with $\mathbf{I}_{n+1}$ the impulse of the nodes in contact defined by: $\mathbf{I}_{n+1} = \Delta t \mathbf{f}_{cont,n+1}$. This formulation allows us to handle the velocity jumps during the first impact and the following contact conditions. The impact vector can also be written as follows:

$$\mathbf{I}_{n+1} = (\mathbf{L}_{N,n+1})^T \lambda_{N,n+3/2} \tag{8}$$

with $\lambda_{N,n+3/2}$ the Lagrange multipliers defined at time $t_{n+3/2}$ and $\mathbf{L}_{N,n+1}$ the restriction operator identifying the degrees of freedom involved in the contact in the normal direction to the interface. Finally, multiplying both sides of Eq. (7) by $\mathbf{L}_{N,n+1}\mathbf{M}^{-1}$, we obtain the dual problem at the interface whose unknowns are the Lagrange multipliers:

$$\mathbf{H}_N \lambda_{N,n+3/2} = \mathbf{b}_{N,n+3/2} \tag{9}$$

where $\mathbf{H}_N$, also known as the Steklov–Poincaré operator, and the right-hand side vector $\mathbf{b}_{N,n+3/2}$, are defined by:

$$\begin{cases} \mathbf{H}_N = \mathbf{L}_{N,n+1}\mathbf{M}^{-1}(\mathbf{L}_{N,n+1})^T \\ \mathbf{b}_{N,n+3/2} = -\mathbf{L}_{N,n+1}\left(\dot{\mathbf{U}}_{n+1/2} + \Delta t \mathbf{M}^{-1}\left(\mathbf{f}_{ext,n+1} - \mathbf{C}\dot{\mathbf{U}}_{n+1/2} - \mathbf{K}\mathbf{U}_{n+1}\right)\right) \end{cases} \tag{10}$$

3. Numerical model

3.1. Two-storey structure models

Finite Element models of the two 5 m high two-floors structures, with steel columns and beams, are depicted in Fig. 2. The masses of Structures 1 and 2 are equal to 9200 kg and 7000 kg, respectively. The concrete slabs have 22 cm of thickness. For the concrete material of the slab, Young's modulus, Poisson's coefficient and density are: $E = 30$ MPa, $\nu = 0.2$ and $\rho = 2400$ kg m^{-3}. For the steel material of the beams, columns and diagonal cross bar bracing, the material characteristics are: $E_s = 200\,000$ MPa, $\nu_s = 0.3$ and $\rho_s = 7800$ kg m^{-3}. Structure 1 is more flexible than Structure 2. More geometric and materials details about the two adjacent structures tested on the shake table AZALEE (CEA, France) and the tested structures can be found in [28].

The pre-processing is made with the FE code Cast3M [44]. Two numerical models are illustrated in Fig. 2. For the first one, the slab is represented by 3D hexahedral elements, whereas, for the second one, the slabs are only represented by shell elements. The first model has been set up to better represent the time history of the impacts and contacts between the two faces of the colliding slabs. The second model is also explored because it is more cost efficient than the first one and shell elements are widely used in practice for modeling slabs in civil engineering structures. In the following, the models are denoted by "Model A" and "Model B", respectively.

We have to make sure that the mesh size is able to reproduce the floor accelerations over a broad band frequency in the investigated pounding situation. We choose the highest frequency as: $f_{max} = 400$ Hz. The P-wave speed in the slab is $c_p = \sqrt{\lambda + 2\mu/\rho}$, where λ and μ are Lamé's coefficients. It gives $c_p \approx 3300$ m/s. The shortest wavelength λ_{min} can be assessed as $\lambda_{min} = c_p/f_{max}$, leading to $\lambda_{min} \approx 11$ m. A minimal "rule of thumb", stated for example in [45], is 10 nodes per wavelength, therefore 1.1m. We adopt a fine FE element size to model the slabs equal to 12 cm which guarantees an accurate numerical prediction of the longitudinal waves.

Moreover, a mesh sensitivity analysis is carried out to ensure the convergence of the results. It is found that a finer mesh has minor changes on the results, especially in terms of floor response spectra, and a coarser mesh can deteriorate the results. Furthermore, for the model with the hexahedral elements (Model A), increasing the number of elements in the thickness does not improve the results due to wave propagation predominantly in the plane of the slab. Thus we model the slab with only one element in the slab thickness for reducing the computation time. In both models, beams and columns are modeled by Euler–Bernoulli beam elements whereas the diagonal cross bracing is modeled by bar elements. The materials are considered in their elastic domain and we adopt the small displacement assumption. Considering Model A, Structures 1 and 2 have 20 520 and 15 528 degrees of freedom (dofs), respectively. For Model B with shell elements, Structure 1 and 2 have 19 464 and 14 664 dofs, respectively. Considering the reference (X, Y, Z) in Fig. 2, the principal direction is according to the longitudinal X axis, the transverse direction corresponds to the Y axis and the vertical axis to the Z axis. During the experimental campaign, the X, Y and Z accelerations of each corner of the shaking table were recorded. The four accelerations are close but yet different. Thus the accelerations, recorded according to the three directions, are averaged and then applied as input accelerations in transient computation.

3.2. Modal analysis

Eigenfrequency discrepancies of the structure models can have significant influence on the time–history results, in particular when impact and contact phenomena occurred [28]. So, in order to minimize the difference between the experimental and numerical eigenfrequencies, the geometric parameters related to two types of elements have been calibrated: first, the section area of cross-bracing bar elements and, second, the section area and inertia moments of the beam elements called here as joint-elements. These latter elements represent the bolted connections between steel beams and columns, illustrated in Fig. 3: only the steel frame is shown, without the concrete slab, with the highlighted joint-elements.

The choice of these two modifications has an intuitive physical meaning. For the first eigenfrequencies in the Y direction and around the Z axis, whenever a bar of the cross bracing bars is pulled, the other bar of the diagonal cross bracing is compressed and, since these bars are very slender, the compressed ones do not increase the stiffer of the frame due to the buckling. In order to consider the possible buckling, we decrease the cross-section area. The second modification concerning the joint-elements can be justified by the fact that the tested structures have strongly bolted rigid connections between beams and columns. This is why stiff beam elements were used at the corners of the steel frame.

The modification of the parameters mentioned above is empirically done in such a way that the eigenfrequencies of the numerical models

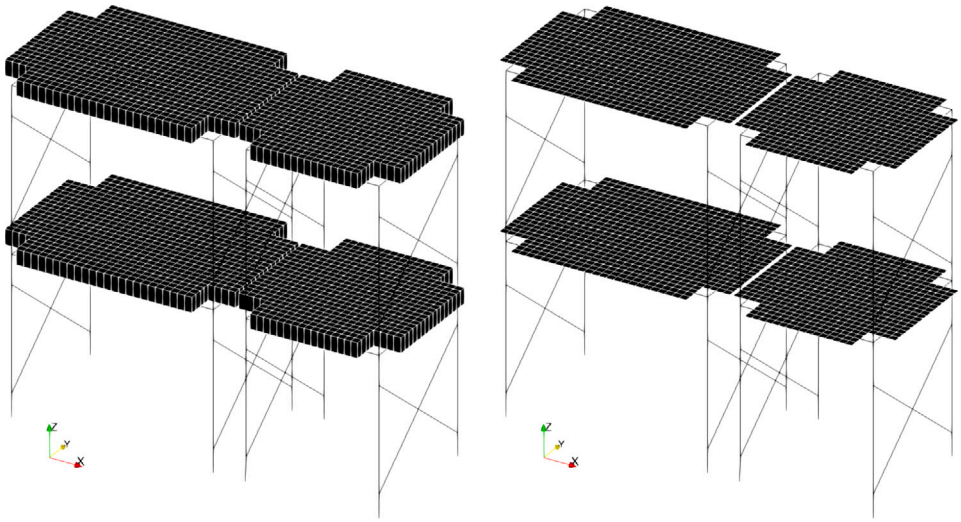

(a) Model A (b) Model B

Fig. 2. Meshes of the colliding structures for the two models with the slab modeled by (a) hexahedral elements and (b) shell elements.

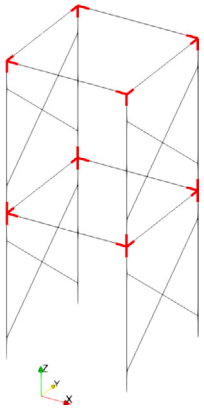

Fig. 3. Steel frame of Structure 2 with highlighted joint-elements (in red).

Table 1
Modal analysis for Models A and B: Comparison between numerical results and experimental data.

		Principal direction		Transverse direction		Rotation around vertical axis	
		1^{st} freq. (Hz)	2^{nd} freq. (Hz)	1^{st} freq. (Hz)	2^{nd} freq. (Hz)	1^{st} freq. (Hz)	2^{nd} freq. (Hz)
I	Experimental	2.1	5.6	6.1	17.5	8.6	24.4
	Model A	2.1	5.6	6.3	18.4	8.6	24.3
	Model B	2.1	5.6	6.4	18.4	8.6	24.3
II	Experimental	3.7	10.3	8.2	25.2	10.2	28.0
	Model A	3.7	10.3	8.4	24.3	10.2	28.1
	Model B	3.7	10.3	8.5	24.4	10.2	28.0

match the experimental ones. Once fixed the parameters from the modal analysis, they are not changed for the following transient simulations with impact/contact phenomena. The results from the modal analysis are summarized in Table 1, which compares the modal analysis results, for the two structures, to the experimental data [28], for the two numerical models.

3.3. Initial gap values between the contacting slabs

An important point about the initial configuration of the two adjacent structures is the presence of geometric defects of the slabs that makes the impacting faces, one of each structure, not parallel [28]. These geometric defects can induce noticeable rotational motion for both structures, even if the torsional response is attenuated thanks to the diagonal cross bracing. The torsional response is excited by the induced eccentric pounding which plays a significant role in the predicted accelerations. As a consequence, these defects observed in the initial configuration of the two colliding structures are introduced in the models. The defect values are different for each configuration of the structures ($gap = 5$ cm, $gap = 2$ cm and $gap = 0$ cm) and were measured during the experimental campaign. Fig. 4 illustrates the geometric defects by giving the distance between the extremities of the impacting faces of the slabs. We assume that the faces in contact are plane, but they are not parallel. If we do not consider the observed defects in the initial slab configuration, the distances A, B, C and D should be equal to 5 cm for the structure configuration of $gap = 5$ cm, and, in the same manner, 2 cm for the $gap = 2$ cm configuration and 0 cm for the $gap = 0$ cm. In order to consider the experimental discrepancies in the initial gap values, the mesh of Structure 2 is slightly modified by shortening or lengthening the elements whose faces are in contact with Structure 1.

3.4. Rayleigh damping in CD explicit time integration

During the experimental campaign, the eigenfrequencies and related damping ratios for both structures are identified [30]. The identified damping values are at about 1.5%. As already mentioned, we use the Rayleigh damping because it is widely used in earthquake simulations in which implicit time integration is classically adopted. Nonetheless, when a lot of impacts occur, the explicit CD time integration can be preferred as in [27], where the explicit code LS-DYNA is employed. The proposed approach, based on the CD-Lagrange scheme presented before, is also explicit and special care has to be taken to ensure the stability by accurately assessing the critical time step. In particular, although Rayleigh damping with a stiffness matrix contribution is very efficient to damp out spurious numerical oscillations coming from the FE discretization and triggering by the impacts, Rayleigh damping also leads to a reduction of the critical time step [40].

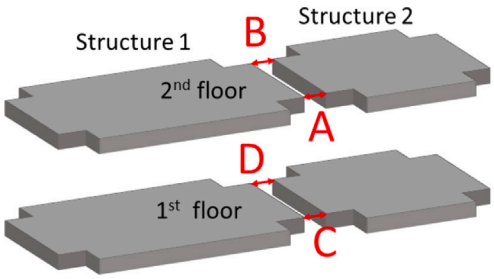

	gap = 5*cm*	gap = 2*cm*	gap = 0*cm*
A (*cm*)	5.5	2.5	0.0
B (*cm*)	5.0	2.0	0.7
C (*cm*)	4.7	1.9	1.7
D (*cm*)	5.0	2.1	1.6

Fig. 4. Distances between the extremities of the impacting faces of the two floors, in the three different gap configurations.

Table 2
Parameters of the Rayleigh damping.

	α	β
Structure 1	0.1562	1.2557×10^{-5}
Structure 2	0.2723	1.2426×10^{-5}

Table 3
PGA of the seismic excitations for each configuration.

	Cadarache	El Centro	Northridge	Kobe
gap = 5 cm	0.45 g	0.35 g	0.20 g	0.20 g
gap = 2 cm	0.20 g	0.15 g	0.10 g	0.20 g
gap = 0 cm	0.15 g	0.15 g	0.10 g	0.15 g

With the Rayleigh damping, expressed as a function of the mass matrix and stiffness matrix as $\mathbf{C} = \alpha\mathbf{M} + \beta\mathbf{K}$, the more the high frequencies are damped out, the more the stability time step is decreased. As a result, the β parameter of the Rayleigh matrix, related to the stiffness matrix, has to be sufficiently high to damp out the numerical oscillations but not too high to not excessively decrease the critical time step. The coefficients of the Rayleigh damping for each structure are presented in Table 2.

First we evaluate the critical time step without damping for the two models A and B. From [40], the critical time step is obtained by:

$$\Delta t_{crit} = \frac{2}{\omega_{max}} \tag{11}$$

with ω_{max} the maximum angular frequency of the finite element mesh obtained by solving the classical eigenvalue problem: $det(\mathbf{K} - \omega^2\mathbf{M}) = 0$. It is important to note here that the assessment of the maximum angular frequency is time consuming. This is why, in explicit dynamics, an upper bound is usually preferred, computed as the ratio of the finite element size and the speed of the pressure wave, known as the Courant–Friedrichs–Lewy (CFL) stability criterion. Here, we compute a more accurate critical time step by solving the eigenvalue problem and computing the maximum angular frequency. The maximum angular frequency between the two Structures 1 and 2 is obtained: $\omega_{max} = 3.05 \times 10^5$ rad s^{-1} for Model A and $\omega_{max} = 1.82 \times 10^5$ rad s^{-1} for Model B.

With Rayleigh damping, the expression for the stable time step for the CD time integration scheme is reduced, accordingly to [40], as:

$$\Delta t_{crit} = \frac{2}{\omega_{max}} \left(\sqrt{1 + \xi_{max}^2} - \xi_{max} \right), \qquad \text{with} \quad \xi_{max} = \frac{\alpha}{2\omega_{max}} + \frac{\beta\omega_{max}}{2} \tag{12}$$

with α and β the Rayleigh parameters of values given in Table 2. As a consequence, the stability time step of the damped Model A becomes 1.58×10^{-6} s, that is 24% of the critical time step of the undamped model, whereas the stability time step of the damped model B becomes 4.16×10^{-6} s, that is 38% of the critical time step of the undamped model. These time steps are kept constant during the whole simulation duration for both structures.

4. Numerical analysis

In earthquake engineering, a practical and widely used way of characterizing floor motions and their effects on internal equipment is based on pseudo-acceleration floor response spectra. Therefore, the floor response spectra are largely investigated in the following results, over a broad frequency range up to 400 Hz. The simulations with pounding are done under four different seismic excitations: Cadarache, El Centro, Northridge and Kobe [28]. The three structure configurations (gap = 5 cm, gap = 2 cm, gap = 0 cm) are considered, giving 12 different cases as resumed in Table 3 with the corresponding peak ground accelerations (PGA).

The results presented in the following are relative to the principal direction (*i.e.* X axis), that is the direction of impacts. Besides, the experimental accelerations of each slab are averaged by considering accelerations recorded by four accelerometers, located close to each corner of the slab. For the numerical results, the acceleration is recorded at the closest nodes of the mesh to accelerometer locations and then they are averaged in the same way as in experimental results. Further details about the experimental campaign can be found in Crozet et al. [28–30].

The simulations are carried out for 25 s of seismic signals. The CD-Lagrange scheme presented before has been implemented in Matlab environment. Meshes and FE models are built in the FE code Cast3M [44]. Mass and stiffness matrices are generated in Cast3M and then exported to Matlab environment for the transient computation with impacts using the CD-Lagrange scheme. Model A, without parallel computation takes 10 h with an Intel i5-6200U with 16 Gb of RAM (regular Notebook) whereas Model B, using the same Notebook, takes 2.5 h.

4.1. Drift and acceleration on the second floor

Fig. 5(a), (c) and (e) present the comparison of the inter-storey normalized displacements (or drifts), related to the second storey, between the numerical and experimental results, in the case of the Northridge excitation and for the three structure configurations. The inter-storey drift of Structure 2 is plotted. As it can be seen, one can notice that the interstorey drifts are well represented by the numerical models.

In Fig. 5(b), (d) and (f), we show the comparison between numerical and experimental accelerations, recorded on the second floor, for different gap configurations. One can clearly see that the number of impacts increases with the decreasing gap. The performance of the explicit computation with the CD-Lagrange scheme is not altered in the case of a zero gap value, when a lot of impacts take place, contrary to classical implicit time integration scheme. Regarding the peak amplitude for the three structure configurations, one can see that, in general, the numerical models are in good agreement with the experimental data.

The comparison between the two numerical models and the experimental pseudo-acceleration floor response spectra, computed at 5%

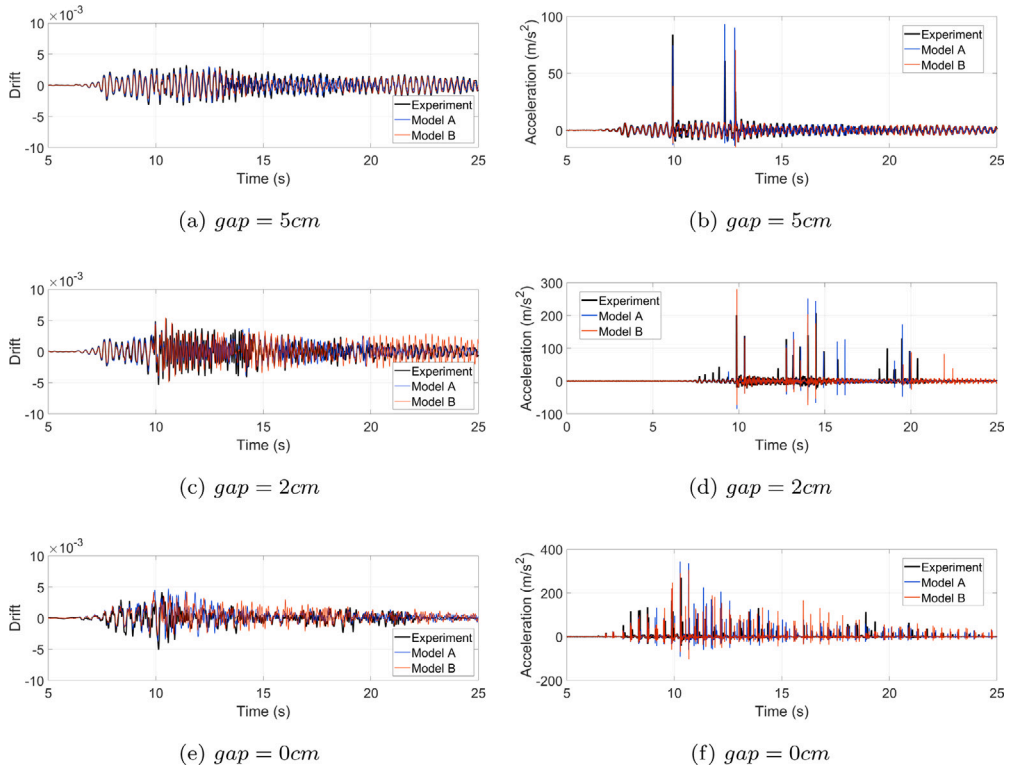

Fig. 5. Inter-storey drift and acceleration of Structure 2 for Kobe excitation and the three different gap configurations.

of damping ratio, is presented in Fig. 6 for the four excitations and the three gap values, at the second floor of Structure 2. In addition, results with Model A, obtained without pounding have been plotted for comparison purposes as well as results using Model A but without any geometric imperfections (symmetric geometry: gap values exactly equal to 5 cm, 2 cm and 0 cm). Globally speaking, it can be observed in Fig. 6 that response spectra predicted by the two Models A and B are consistent with each other. In the low frequency range, response spectra exhibit two first peaks, at 3.7 Hz and 10.3 Hz, corresponding to the first eigenfrequencies of Structure 2 in the longitudinal direction. In the high frequency range, the acceleration peaks generated by the impacts, determine the shape of the response spectrum. Obviously, the model without pounding fails to reproduce the experimental floor response spectra and the comparison with the other models highlights the impact effect in the high frequency range. The model without any geometric imperfections is able to reproduce this high frequency branch, characteristics of the impacts between the slabs, but it can be seen that this branch is higher than the one related to the experimental data. On the contrary, by taking into account the geometric imperfections concerning the gap values along the impacting faces of the slabs as given in Fig. 4, it is shown that results from Models A and B are closer to the high frequency branch related to the experimental data. It underlines the significant role of the eccentricity for reproducing the accelerations recorded at the slabs. The relation between the high frequency branch in the response spectrum and the acceleration peaks has already been explored by Crozet et al. [8], considering a simplified case of a single degree of freedom oscillator. In the following, thanks to the refined FE mesh and the simulation of eccentric pounding, the shape of the high frequency branch in the response spectrum is further investigated by studying the influence of the peaks in the acceleration time–history. In particular we focus on the peak corresponding to the largest impulse, computed as the integration in time of the slab acceleration.

4.2. Acceleration peak influence on the pseudo-acceleration

By analyzing spring–mass systems, Crozet et al. [8] observed that, in the case of pounding, high impulsive impacts govern the pseudo-acceleration response spectra in the high frequency range. Moreover, the authors observed that, besides the value of the impact impulse, the impact duration has also considerable influence. Despite the simplicity of the systems employed in [8], these results remain true for more complex models as the ones under consideration.

The contact duration related to an impulse corresponds to the time period during which the slabs are in contact. Thanks to the CD-Lagrange scheme, the impact time between the slabs for each acceleration peak is easily obtained and does not depend on contact stiffness or damping parameters, as it is the case when adopted traditional contact elements for pounding.

To assess the influence of acceleration peaks on the shape of the high frequency branch in the response spectrum, we consider in Fig. 7 different signal treatment procedures of the time–history numerical acceleration obtained with Model A, before computing the response spectrum. The first treatment is the complete acceleration time–history without any change, called “Complete”. The second one, denoted in Fig. 7(a) by “All peaks”, gathers all the peaks in the time–history acceleration, but the accelerations are set to zero between the peaks. In the third treatment, only the peak with the highest impulse is kept and it is called the “Highest impulsive peak” in Fig. 7(b). For the sake of comparison, the fourth treatment corresponds to the complete time–history acceleration but without the peaks, called “Without peaks” in Fig. 7(c). One last treatment is considered in the analysis: a Dirac pulse in acceleration having the same impulse as the highest impulsive peak in the third treatment but with a very short duration. More precisely, the duration of the Dirac is equal to twice the time step in the explicit time integration (one time step for the increase to the peak value and another one for the decrease to the zero value). The purpose is to explore the effect of the contact duration on the shape of the floor response spectra.

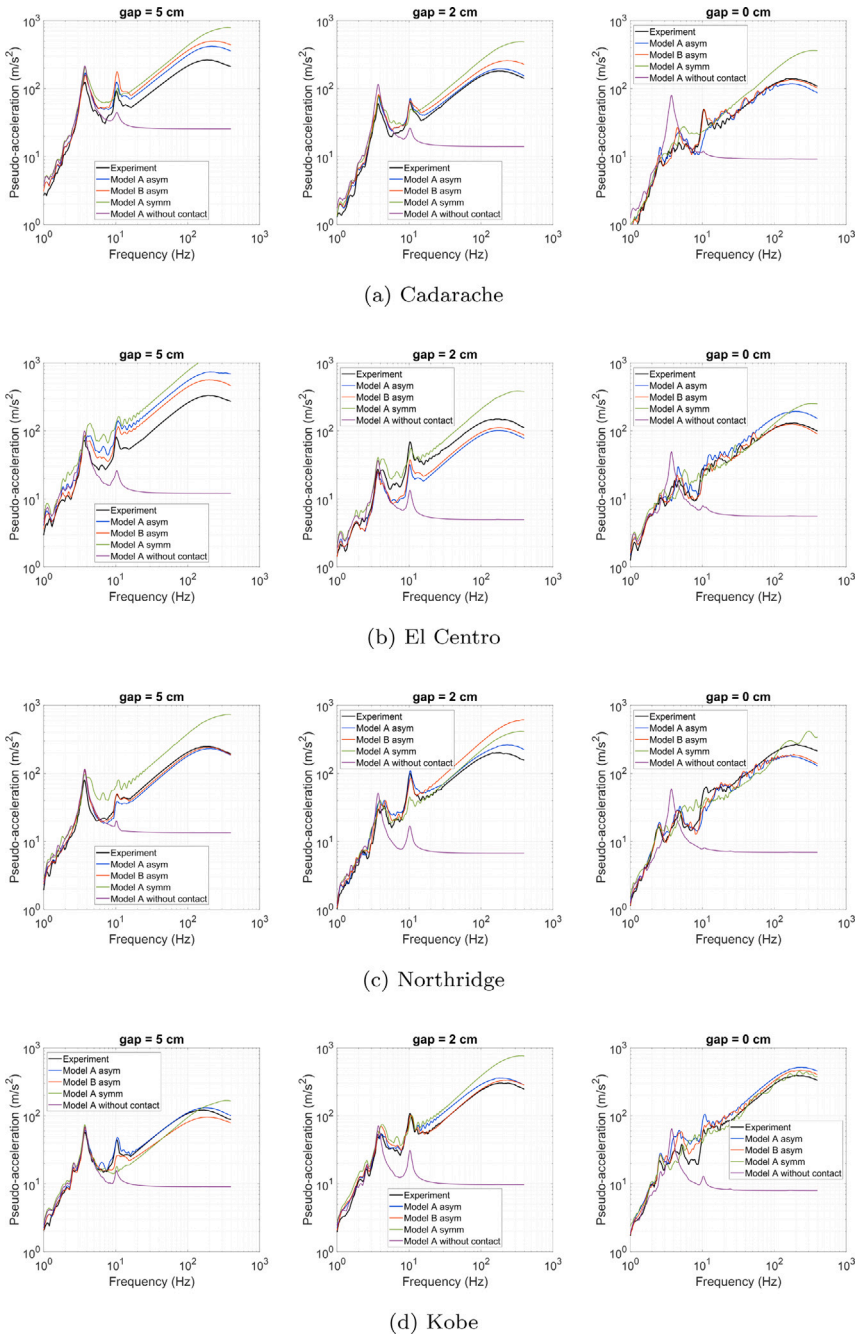

Fig. 6. Floor response spectra (computed at 5% of damping) at the second floor of Structure 2 under (a) Cadarache, (b) El Centro, (c) Northridge and (d) Kobe excitation with different gap values. Model A and B asymmetric (with geometric imperfections), Model A symmetric (without any geometric imperfections) and Model A asymmetric without pounding.

Fig. 8 shows the floor response spectra, for the five previous treatments, for all 12 cases (three gap values and four excitations). The comparison between the "Complete" curve against the "All peaks" one highlights the strong influence of the acceleration peaks on the high frequency branch of the response spectrum. Indeed, the response spectra computed from the modified signals containing all the peaks are very close, in the high frequency range, to the ones from the complete time–history excitation, and this observation can be checked for all the 12 cases investigated. When we compare the pseudo-acceleration spectra related to the complete time–history to the ones computed from only the highest impulsive peak, the match is always very good in the high frequency range. This means that the acceleration of the highest impact impulse mainly governs the high frequency branch of the response spectrum. Finally, regarding the response spectra, computed from the Dirac pulse characterized by the same impulse as the previous highest impulse, it is possible to notice that the match is quite good over a certain frequency range and then deviates from the complete response spectra which tend to smoothly decrease in the highest frequency range, at around 250 Hz. It clearly shows that the high frequency branch of the response spectra depends on the impulse but also on the contact duration.

To conclude about Fig. 8, the comparison between the above treatments on time–history acceleration highlights the strong influence of the acceleration peaks on the response spectrum, requiring an accurate representation of the pounding phenomena. Not only the impulse associated with the impact need to be well reproduced, but also the contact duration. An impact with very small duration will strongly

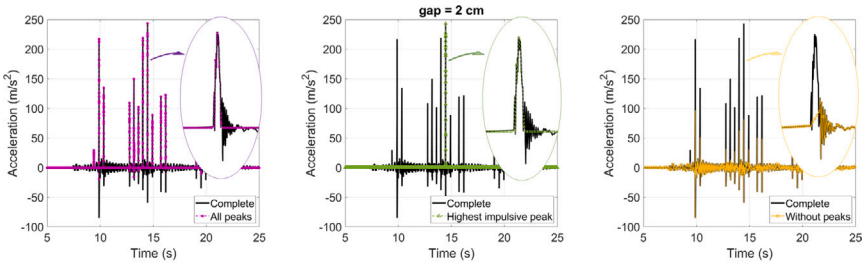

Fig. 7. Three different treatment procedures applied on numerical time–history acceleration (a) with only the peaks, (b) with only the peak with the highest impulse and (c) without any peak.

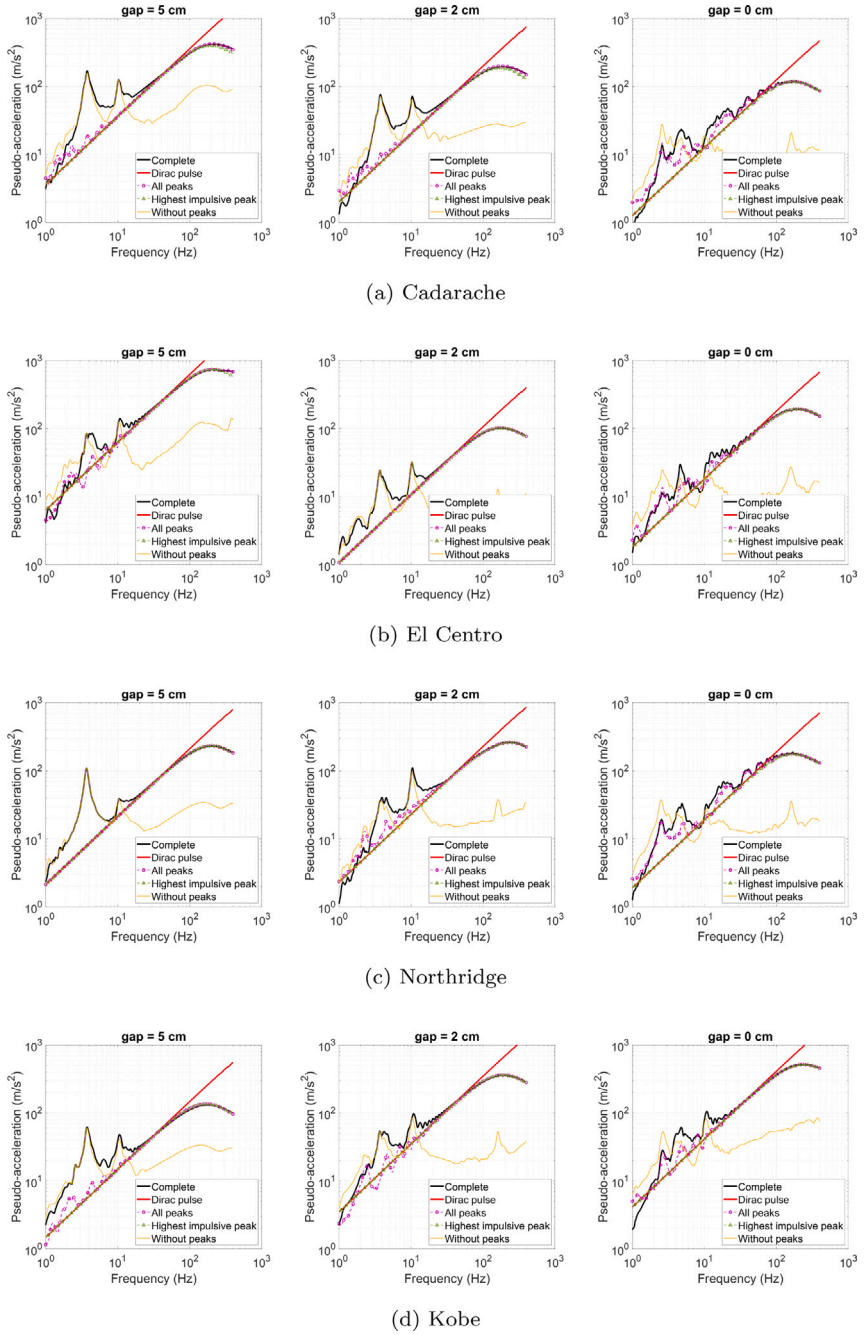

Fig. 8. Response spectra (at 5% damping) for the four post-treatment procedures applied on the time–history acceleration at the second floor of Structure 2 under (a) Cadarache, (b) El Centro, (c) Northridge and (d) Kobe excitation with different gap values.

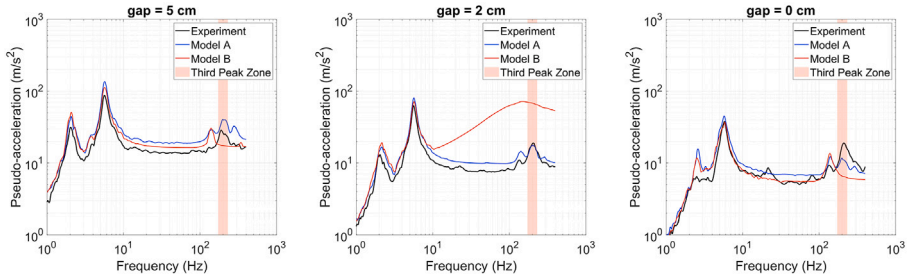

(a) Cadarache

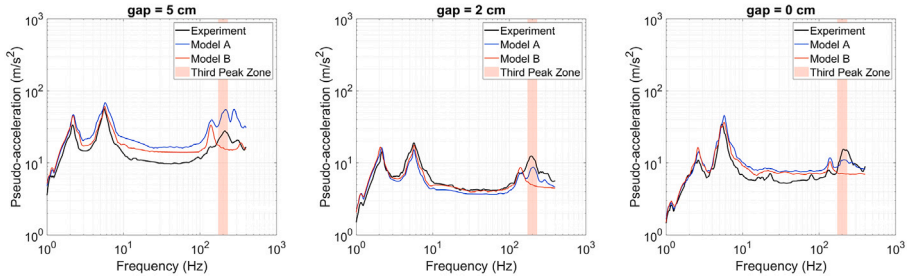

(b) El Centro

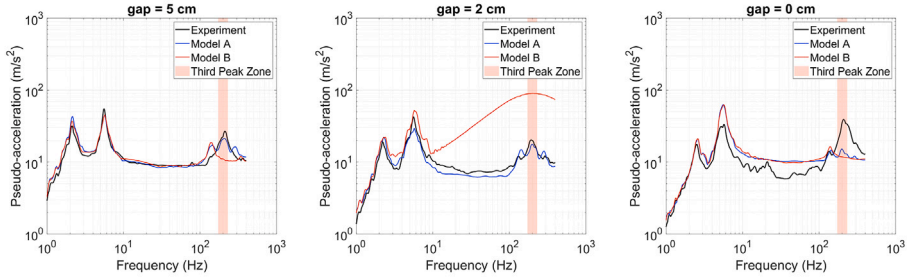

(c) Northridge

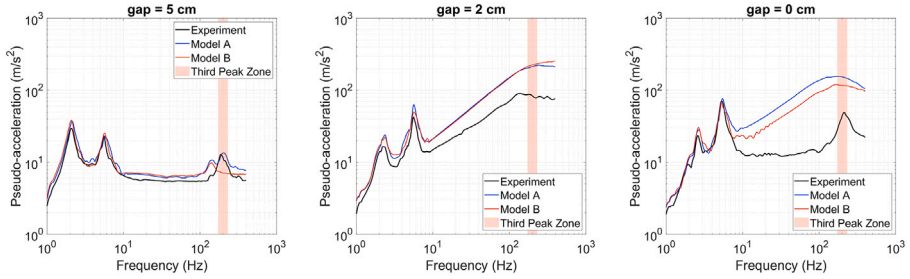

(d) Kobe

Fig. 9. Response spectra (at 5% damping) at the first floor of Structure 1 for $gap = 5$ cm, $gap = 2$ cm and $gap = 0$ cm configurations.

excite the high frequencies. The comparison between the numerical and experimental results in Fig. 6 puts in evidence that the used algorithm for the impact simulation, the CD-Lagrange scheme [35], is able to well predict the eccentric pounding, with no significant discrepancies between the two Models A and B. Nonetheless, it has to be stressed that Model A is able to take into account contacting points over all the surface of the contacting face of the slabs, including left–right eccentric pounding but also the ability to impact successively the top and bottom points of the surface. This advantage of Model A over Model B will be highlighted in the following by focusing on floor response spectra at the first floor.

4.3. Impact influence on the first floor

The impact is detected on the second floor of Structure 2 for all the 12 cases of Table 3, as shown in Fig. 8. However, at the first floor, the impact is only detected in a few cases. As showed previously, the acceleration peaks due to the impacts are the most influential quantities on the high frequency branch of the response spectrum. Here, on the first floor, even without impacts between the slabs, some high frequency response can be observed as shown in Fig. 9 where the response spectra of the first floor of Structure 1 are plotted for all the 12 cases. The two first peaks represent the two first eigenfrequencies of Structure 1 in the longitudinal direction, at 2.1 Hz and 5.6 Hz. The two first peaks are well captured in frequency and in amplitude by both

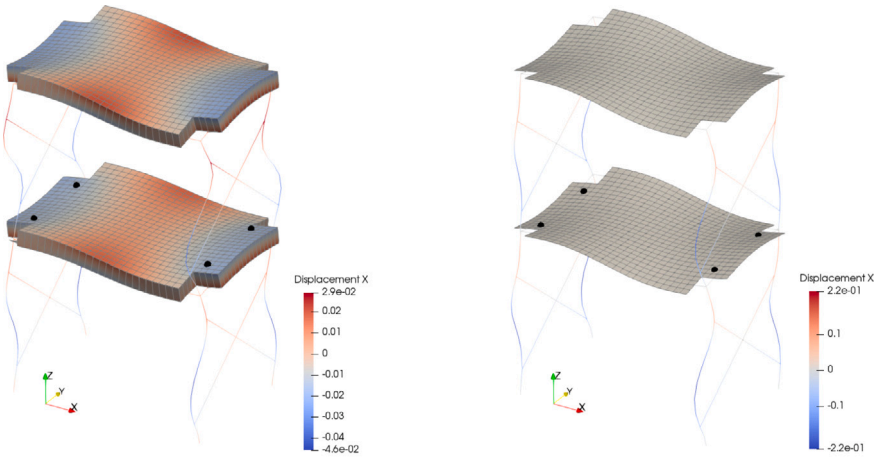

(a) (b)

Fig. 10. Amplified anti-symmetric slab mode with eigenfrequency close to 200 Hz with the nodes locations (black dots) for (a) Model A and (b) Model B.

numerical models. However, we can observe that there is a third peak, near 200 Hz, highlighted by a vertical red strip, which is predicted by Model A, with hexahedral FE elements, but not by Model B, with shell FE elements. It has to be noted that, in a few cases, for example for Model A with $gap = 2$ cm and Kobe signal, the third peak does not appear because impacts are predicted at the first floor: then, the response spectra are characterized by a high frequency branch and the third peak cannot be observed.

The experimental results show a peak in response spectra close to 200 Hz, which is explained by Crozet et al. [28] as an anti-symmetric slab mode, with respect to the Y axis. This mode for the two numerical models is illustrated in Fig. 10 with the black dots representing the recorded node locations in the numerical model. It is shown that the middle plane of the slab, which is what Model B represents, has a zero displacement in the X direction. What makes this slab mode significant for the response spectra close to 200 Hz in the X direction, is the location of the nodes at which the accelerations are recorded. Indeed, in the experimental campaign, the accelerations are recorded on the upper part of the slab. Model A with hexahedral elements approximately adopts the same recording points as in the experimental campaign but it is not the case of Model B for which the recording points are located in the medium plane of the shell elements.

5. Conclusions

The proposed numerical approach, based on an explicit time integration and Lagrange multipliers (CD-Lagrange scheme), is able to reproduce the response of two colliding structures dynamically tested in a well documented experimental campaign, in terms of displacements and accelerations with a special focus on the pseudo-acceleration floor response spectra. Floor response spectra are predicted over a wide frequency range, up to 400 Hz. The eccentric pounding is simulated for different earthquake excitations and different gap configurations, characterized by a small number of impacts ($gap = 5$ cm configuration) to a large number of impacts ($gap = 0$ cm configuration). The analysis of the acceleration peaks on the second floor indicates that the numerical approach is able to well represent the impacts, characterized by their impulse and duration, which govern the high frequency branch of the floor response spectra. There is no need of parameter tuning inherent to contact elements usually employed in pounding analyses, demonstrating the robustness of the proposed approach based on the explicit CD-Lagrange scheme. Floor response spectra obtained from the two investigated models (slabs modeled with hexahedral or shell elements) are consistent between each other. It was shown that some slab vibration modes, not reproduced by the model based on shell elements, have been detected by the model with hexahedral elements. Nonetheless, the computation time related to the model with hexahedral elements is 4 times bigger than the one related to shell elements due to the higher number of degrees of freedom and lower time steps in explicit computations. Work is in progress to apply the proposed numerical approach to $in-situ$ adjacent electrical buildings representative of a nuclear power plant.

CRediT authorship contribution statement

José Henrique Krahenbuhl Ambiel: Conceived of the presented idea, Developed the theory, Implemented the algorithms and performed the computations, Writing – oiginal draft. **Michael Brun:** Conceived of the presented idea, Developed the theory, Writing – original draft. **Alfred Thibon:** Supervision. **Anthony Gravouil:** Developed the theory, Contributed to the final version.

Declaration of competing interest

The authors declare that they have no known competing financial interests or personal relationships that could have appeared to influence the work reported in this paper.

Acknowledgments

The research was supported by Electricité de France. This support is greatly acknowledged. The authors would like to thank V. Crozet, CEA, France, for providing the experimental data of the IBB campaign carried out on the shake table AZALEE.

References

[1] Rosenblueth E, Meli R. The 1985 earthquake: Causes and effects in Mexico city. Concr Int 1986;8(5):23–34.
[2] Bertero VV. Observations on structural pounding. In: The Mexico earthquake - 1985: Factors involved and lessons learned. ASCE; 1987, p. 264–78.
[3] Kasai K, Maison BF. Building pounding damage during the 1989 Loma Prieta earthquake. Eng Struct 1997;19(3):195–207.
[4] Cole GL, Dhakal RP, Turner FM. Building pounding damage observed in the 2011 Christchurch earthquake. Earthq Eng Struct Dyn 2012;41(5):893–913.
[5] Kasai K, Jeng V, Patel PC, Munshi JA, Maison BF. Seismic pounding effects-survey and analysis. Earthq Eng 1992.
[6] Jankowski R. Non-linear viscoelastic modelling of earthquake-induced structural pounding. Earthq Eng Struct Dyn 2005;34(6):595–611.
[7] Jankowski R, Mahmoud S. Earthquake-induced structural pounding. Springer; 2015.

[8] Crozet V, Politopoulos I, Yang M, Martinez J-M, Erlicher S. Sensitivity analysis of pounding between adjacent structures. Earthq Eng Struct Dyn 2018;47(1):219–35.
[9] Anagnostopoulos SA. Pounding of buildings in series during earthquakes. Earthq Eng Struct Dyn 1988;16(3):443–56.
[10] Athanassiadou CJ, Penelis GG, Kappos AJ. Seismic response of adjacent buildings with similar or different dynamic characteristics. Earthq Spectra 1994;10(2):293–317.
[11] Davis RO. Pounding of buildings modelled by an impact oscillator. Earthq Eng Struct Dyn 1992;21(3):253–74.
[12] Naderpour H, Barros RC, Khatami SM, Jankowski R. Numerical study on pounding between two adjacent buildings under earthquake excitation. Shock Vib 2016;2016:1504783.
[13] Khatami SM, Naderpour H, Barros RC, Jakubczyk-Galczynska A, Jankowski R. Effective formula for impact damping ratio for simulation of earthquake-induced structural pounding. Geosciences 2019;9, 347:1:15.
[14] Elwardany H, Seleemah A, Jankowski R. Seismic pounding behavior of multi-story buildings in series considering the effect of infill panels. Eng Struct 2017;144:139–50.
[15] Maison BF, Kasai K. Analysis for a type of structural pounding. J Struct Eng 1990;116(4):957–77.
[16] Maison BF, Kasai K. Dynamics of pounding when two buildings collide. Earthq Eng Struct Dyn 1992;21(9):771–86.
[17] Anagnostopoulos SA, Spiliopoulos KV. An investigation of earthquake induced pounding between adjacent buildings. Earthq Eng Struct Dyn 1992;21(4):289–302.
[18] Raheem SE Abdel. Seismic pounding between adjacent building structures. Electron J Struct Eng 2006;6(66):155.
[19] Karayannis CG, Favvata MJ. Earthquake-induced interaction between adjacent reinforced concrete structures with non-equal heights. Earthq Eng Struct Dyn 2005;34(1):1–20.
[20] Favvata MJ, Naoum MC, Karayannis CG. Earthquake induced interaction between RC frame and steel frame structures. WIT Trans Built Environ 2013;134:839–51.
[21] Favvata MJ. Minimum required separation gap for adjacent RC frames with potential inter-story seismic pounding. Eng Struct 2017;152:643–59.
[22] Wolf JP, Skrikerud PE. Mutual pounding of adjacent structures during earthquakes. Nucl Eng Des 1980;57(2):253–75.
[23] Leibovich E, Rutenberg A, Yankelevsky DZ. On eccentric seismic pounding of symmetric buildings. Earthq Eng Struct Dyn 1996;25(3):219–33.
[24] Papadrakakis M, Apostolopoulou C, Zacharopoulos A, Bitzarakis S. Three-dimensional simulation of structural pounding during earthquakes. J Eng Mech 1996;122(5):423–31.
[25] Jankowski R. Non-linear FEM analysis of earthquake-induced pounding between the main building and the stairway tower of the Olive View Hospital. Eng Struct 2009;31(8):1851–64.
[26] Karayannis CG, Naoum MC. Torsional behavior of multistory RC frame structures due to asymmetric seismic interaction. Eng Struct 2018;163:93–111.
[27] Bi K, Hao H. Numerical simulation of pounding damage to bridge structures under spatially varying ground motions. Eng Struct 2013;46:62–76.
[28] Crozet V, Politopoulos I, Chaudat T. Shake table tests of structures subject to pounding. Earthq Eng Struct Dyn 2019;48(10):1156–73.
[29] Crozet V, Politopoulos I, Chaudat T. Shake table test of large scale structures subject to pounding. In: 16th European conference on earthquake engineering. 2018.
[30] Crozet V. Etude de l'entrechoquement entre bâtiments au cours d'un séisme (Ph.D. thesis), Institut Polytechnique de Paris; 2019.
[31] Papadrakakis M, Mouzakis H, Plevris N, Bitzarakis S. A Lagrange multiplier solution method for pounding of buildings during earthquakes. Earthq Eng Struct Dyn 1991;20(11):981–98.
[32] Papadrakakis M, Mouzakis HP. Earthquake simulator testing of pounding between adjacent buildings. Earthq Eng Struct Dyn 1995;24(6):811–34.
[33] Muthukumar S, DesRoches R. A Hertz contact model with non-linear damping for pounding simulation. Earthq Eng Struct Dyn 2006;35(7):811–28.
[34] Langlade T, Bertrand D, Grange S, Candia G, de la Llera JC. Modelling of earthquake-induced pounding between adjacent structures with a non-smooth contact dynamics method. Eng Struct 2021;241:112426.
[35] Fekak F-E, Brun M, Gravouil A, Depale B. A new heterogeneous asynchronous explicit–implicit time integrator for nonsmooth dynamics. Comput Mech 2017;60(1):1–21.
[36] Stasio J Di, Dureisseix D, Gravouil A, Georges G, Homolle T. Benchmark cases for robust explicit time integrators in non-smooth transient dynamics. Adv Model Simul Eng Sci 2019;6(1):1–31.
[37] Brun M, Rezakhani R, Molinari J-F. Explicit dynamic approach for unbounded domains in frictional contact with Rate and State laws. Finite Elem Anal Des 2020;174:103402.
[38] Moreau J-J. Unilateral contact and dry friction in finite freedom dynamics. In: Nonsmooth mechanics and applications. Springer; 1988, p. 1–82.
[39] Moreau J-J. Numerical aspects of the sweeping process. Comput Methods Appl Mech Engrg 1999;177:329–49.
[40] Belytschko Ted, Liu Wing Kam, Moran Brian, Elkhodary Khalil. Nonlinear finite elements for continua and structures. John Wiley & Sons; 2013.
[41] Hulbert GM, Chung J. Explicit time integration algorithms for structural dynamics with optimal numerical dissipation. Comput Methods Appl Mech Engrg 1996;137(2):175–88.
[42] Noh G, Bathe KJ. An explicit time integration scheme for the analysis of wave propagations. Comput Struct 2013;129:178–93.
[43] Jean Michel. The non-smooth contact dynamics method. Comput Methods Appl Mech Engrg 1999;177(3–4):235–57.
[44] Cast3m. 2018, http://www-cast3m.cea.fr/.
[45] Zienkiewicz OC, Taylor RL. The finite element method for solid and structural mechanics. Elsevier; 2005.